Nano Research

Open Access

Research Article

High-entropy layered hydroxide nanocatalysts via *in-situ* etching-growth of ZIF-67 for robust hydrogen generation from concentrated $NaBH_4$ solution

Xin Chen[1], Zhenyu Wang[1], Hui Yao[1], Mingjie Jia[1], Yiming Wang[1] ✉, Die Shao[1], Na Ju[1], Yao Wang[1], Zilong Liu[1], Guangwen Xu[2], Yongjian Ai[3] ✉, and Hong-bin Sun[1] ✉

[1] *Department of Chemistry, Northeastern University, Shenyang 110819, China*
[2] *Key Laboratory on Resources Chemicals and Materials of Ministry of Education, Shenyang University of Chemical Technology, Shenyang 110142, China*
[3] *Food Laboratory of Zhongyuan, Key Laboratory of Precision Nutrition and Food Quality, Department of Nutrition and Health, China Agricultural University, Beijing 100193, China*

Cite this article: *Nano Research*, **2026**, *19*, 94908464. https://doi.org/10.26599/NR.2026.94908464

ABSTRACT: Sodium borohydride ($NaBH_4$) solution is a promising liquid "fuel" for continuous hydrogen supply through catalytic hydrolysis, offering a safer alternative to compressed hydrogen to fuel cells. However, the harsh thermal and chemical environments of concentrated $NaBH_4$ hydrolysis cause rapid catalyst deactivation. Herein, we synthesized a high-entropy layered hydroxide (HELH, FeCoNiCuZn@ZIF-67 (ZIF-67 = zeolitic imidazolate framework-67)) nanocatalyst via an *in-situ* etching-growth strategy with ZIF-67. The mechanical structure of residual ZIF-67 inside ensures the robustness of active centers and particles. The efficiency of hydrogen generation is guaranteed by the synergy of different metals in high-entropy structures, which involves borohydride adsorption and H_2 release. Benefiting from this cooperative architecture, the HELH catalyst achieves a high hydrogen generation rate of 8 $L \cdot min^{-1} \cdot g^{-1}$ in a 25 wt.% $NaBH_4$ solution. Density functional theory and electrochemical analyses reveal that abundant oxygen vacancies and multi-metal synergy optimize water activation and lower the reaction barrier. This work provides an effective strategy for designing robust high-entropy catalysts for extreme conditions.

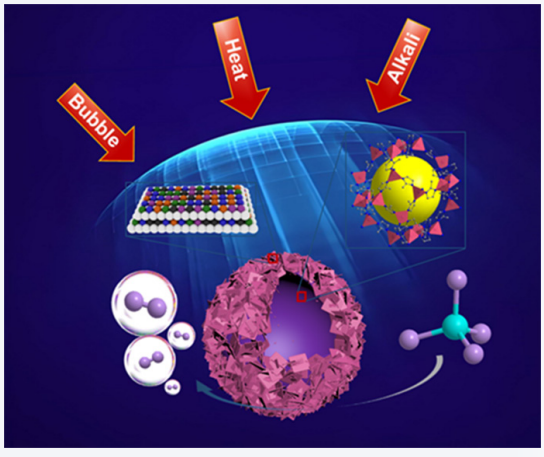

KEYWORDS: high-entropy materials, hydrogen generation, sodium borohydride hydrolysis, metal-organic framework (MOF)-derived catalyst, layered hydroxide, *in-situ* etching-growth

1 Introduction

Hydrogen fuel cells are ideal power sources for unmanned aerial vehicles (UAV) due to the advantages of lightweight and low noise [1–3]. However, the conventional H_2 supply of compressed hydrogen tank has drawbacks such as high risk, low energy density, and inconvenient long-distance refueling [4–7], which severely limits its deployment in complex environments such as disaster rescue missions, field operations, and military actions [8–10]. In contrast, sodium borohydride ($NaBH_4$) is an appropriate hydrogen carrier for emergency supply because of its stable physicochemical properties, a high theoretical hydrogen storage capacity, and the easiness of generating high-purity hydrogen via catalytic hydrolysis [11–13]. Moreover, the reported efficient and cost-effective regeneration methods pave the way for broadening the future application landscape of $NaBH_4$ [14–16].

Although noble metal catalysts have excellent activity towards $NaBH_4$ hydrolysis [17–19], noble-metal-free catalysts are more economical but generally less active [20–23]. Currently, most reported catalysts are evaluated under dilute $NaBH_4$ solution systems [24–26], which leads to reduced fuel energy density.

Received: November 25, 2025; **Revised:** January 14, 2026
Accepted: January 16, 2026

✉Address correspondence to Yiming Wang, 836961227@qq.com; Yongjian Ai, ayj@cau.edu.cn; Hong-bin Sun, sunhb@mail.neu.edu.cn

Concentrated solution systems are necessary for practical applications. However, as illustrated in Eq. (1), the hydrolysis of concentrated $NaBH_4$ solution is accompanied by intense local high temperatures and vigorous bubble release [27, 28], which can severely damage the structure of the catalyst. Facing such adverse working conditions, how to enhance both the catalytic activity and stability is a core challenge for the practical application of noble metal free catalyst.

$$NaBH_4(s) + 2H_2O(1) = NaBO_2(s) + 4H_2(g)$$
$$\Delta H = -210.82\ kJ \cdot mol^{-1} \quad (1)$$

The development of high-entropy catalysts (HECs) offers a new pathway to address this challenge. HECs can significantly promote the catalytic reactions through the synergistic effect of multiple metal active sites and plenty of unsaturated defects [29]. Moreover, the high configurational entropy brings about lattice stability that contributes to the material's robustness under various conditions [30]. These merits are further amplified in high-entropy layered hydroxides (HELHs), which combine the benefits of HECs with intrinsic hydrophilicity and alkaline resistance, making them exceptionally suitable for $NaBH_4$ hydrolysis [14, 31, 32]. To provide a stable scaffold for these active HELHs, metal-organic frameworks (MOFs) like ZIF-67 are ideal candidate precursor. Their ordered metal–ligand networks can serve as both metal resource and reinforcing supports for deriving catalysts [33]. Some research has demonstrated that MOFs exhibit extraordinary structural stability as carriers in the $NaBH_4$ hydrolysis [34, 35]. Additionally, the strategy of constructing layered hydroxides on MOF substrates has already proven advantageous in fields such as electrocatalysis and electrochemical energy storage [36–38]. Given these attributes, *in-situ* growth of HELHs on MOF scaffolds is an ideal strategy to create a tightly integrated, highly durable, and active catalyst.

Herein, we developed FeCoNiCuZn HELH catalyst derived from ZIF-67 through an *in-situ* etching-growth transformation. The resulting hollow nanospheres reserved part of MOFs structure as the internal support, which stabilizes the high-entropy hydroxide shell. The catalyst achieves a hydrogen generation rate of 8 $L \cdot g^{-1} \cdot min^{-1}$ in 25 wt.% $NaBH_4$ at 70 °C and excellent reusability. Combined experiments and theoretical calculations reveal that the collaboration of diverse metals in the HELH facilitates adsorbing BH_4^- and desorbing H_2 to promote the efficient progress of the reaction. Moreover, the abundant oxygen vacancies in the material help adsorb water, thereby accelerating the hydrolysis process.

2 Experimental

2.1 Materials and chemicals

All chemicals and reagents used were of analytical grade and were used without further purification. 2-Methylimidazole (2-MeIm), cobalt nitrate hexahydrate ($Co(NO_3)_2 \cdot 6H_2O$), iron nitrate nonahydrate ($Fe(NO_3)_3 \cdot 9H_2O$), and copper nitrate trihydrate ($Cu(NO_3)_2 \cdot 3H_2O$) were supplied by Aladdin Reagent Co., Ltd., China. Methanol was provided by the Tianjin Yongda Chemical Reagent Co., Ltd., China. The following chemicals were purchased from Sinopharm Chemical Reagent Co., Ltd., China: Nickel nitrate hexahydrate ($Ni(NO_3)_2 \cdot 6H_2O$), zinc nitrate hexahydrate ($Zn(NO_3)_2 \cdot 6H_2O$), sodium hydroxide (NaOH), hydrochloric acid (HCl), ethanol, and sodium borohydride ($NaBH_4$).

2.2 Analytical methods

The surface morphologies of the materials were characterized by a scanning electron microscope (SEM; SU-8000) operated at 5.0 kV and transmission electron microscopy (TEM; JEM2100PLUS, JEOL, Japan) operated at 200 kV and room temperature. Fourier transform infrared (FTIR; Micromeritics ASAP, USA) spectroscopy and powder X-ray diffraction (XRD; Empyrean, PANalytical B.V., Netherlands) patterns were utilized to characterize the chemical structure of catalyst. N_2 physisorption isotherm was measured on an ASAP 2020 absorptiometer (Micromeritics, USA) at 77 K. The Brunauer–Emmet–Teller (BET) was tested to obtain the specific surface area of the samples, and the Barret–Joyner–Halenda (BJH) method was used to gain the pore-size distribution based on the desorption data. An X-ray photoelectron spectroscope (XPS; AXIS Supra, Kratos, USA) was employed to analyze the surface chemical composition, with the binding energy calibrated against the C 1s at 284.6 eV with an experimental error of ±0.2 eV. Inductively coupled plasma optical emission spectrometry (ICP-OES) was performed using an Agilent 5110 instrument (Agilent Technologies Inc., USA), utilizing aqua regia to dissolve the catalyst. The measurements were performed with a radio frequency power of 1150 W at a wavelength of 340.458 nm.

2.3 Catalyst preparation

2.3.1 *Preparation of ZiF-67*

ZIF-67 was synthesized according to the procedure reported with minor modifications [39]. First, a potion of 0.582 g $Co(NO_3)_2 \cdot 6H_2O$ and 0.985 g 2-MeIm was separately dissolved in 40 mL of methanol to obtain the salt solution and ligand solution, respectively. Afterwards, the salt solution was rapidly added to the ligand solution. After stirring at room temperature for 24 h, the product was centrifuged and washed three times with methanol. Finally, the product was dried overnight in a vacuum oven at 60 °C and then finely ground for later use. To facilitate practical utilization, ZIF-67 can also be grown on nickel foam, which was pretreated with dilute hydrochloric acid (0.1 M), ethanol, and deionized water, sequentially.

2.3.2 *Preparation of HELH*

To prepare the NiCoFeCuZn HELH framework, 50 mg of ZIF-67 was dispersed in 10 mL of ethanol containing four metal nitrates (0.1 mmol Ni^{2+}, 0.15 mmol Zn^{2+}, 0.025 mmol Fe^{3+}, and 0.05 mmol Cu^{2+}). After ultrasonication for 5 min, the mixture was transferred to an oven and maintained at 90 °C for 2.5 h. The resulting product was then separated by centrifugation and washed three times with ethanol. Finally, it was dried in a vacuum oven at 80 °C for 12 h. Bimetallic (Bi-), trimetallic (Tri-), and tetrametallic (Tetra-) layered hydroxides (LH) were synthesized using a similar method by varying the types and concentrations of metal salts in the ethanol solution.

2.4 Catalyst activity test conditions

A portion of 5 mL solution containing 25 wt.% $NaBH_4$ and 3M NaOH was injected into a 25 mL round-bottom flask and then placed in an oil bath. After reaching 70 °C, 5 mg catalyst was placed in the solution. The volume of gas produced was measured using the drain gas collection method.

2.5 Kinetics tests for hydrolysis of $NaBH_4$ over catalysts

The reactions were carried out with vigorous stirring at the temperatures of 50, 60, 70 and 80 °C.

The kinetic curves were fitted with a pseudo zero(th) order reaction, and the good linear correlation coefficient confirms the zero(th) order assumption. The kinetic constants are calculated according to the equation

$$C = kt \quad (2)$$

where C is the concentration of $NaBH_4$ consumed at reaction time t and k is the rate constant.

In addition, apparent activation energy (E_a) is calculated by the Arrhenius equation

$$\ln k = -\frac{E_a}{RT} + \ln A \quad (3)$$

where k is the rate constant; A is the pre-exponential factor; R is the molar gas constant (8.314 J·mol^{-1}·K^{-1}); T is the reaction temperature (K).

3 Results and discussion

3.1 Characterization of catalyst

The schematic illustration in Fig. 1(a) outlines the material preparation process. Firstly, the precursor ZIF-67 was synthesized via room-temperature stirring, and its morphology exhibits a truncated octahedron with a uniform particle size of about 250 nm (Figs. 1(b) and 1(c)). The XRD pattern of ZIF-67, consistent with the simulation pattern, confirms the successful synthesis (Fig. S1 in the Electronic Supplementary Material (ESM)). Subsequently, the HELH hollow spheres were fabricated via solvothermal treatment of ZIF-67 dispersed in an ethanol solution containing four metal nitrate precursors (Fe^{3+}, Ni^{2+}, Cu^{2+}, and Zn^{2+}), whose amounts were adjusted according to their solubility product constants (K_{sp}, Table S1 in the ESM). From the SEM (Figs. 1(b)–1(d)) and Fig. S3 in the ESM) and TEM images (Figs. 1(e)–1(h)), it can be clearly seen that the microstructure of the material is in hollow nanospheres morphology of around 300 nm, which indicates that the HELH was obtained by *in-situ* etching-growth using ZIF-67 as a template. This synthetic method ensures that layered hydroxide firmly adheres to the surface of MOFs to prevent its detachment. As highlighted in the blue circle in Fig. 1(f), the outer shell of the material displays lamellar structure characteristic of layered hydroxides. At higher magnification, the crystal lattice fringes with a spacing of 2.54 Å and some amorphous regions can be observed (Fig. 1(g)). In addition, the EDS elemental mapping in Fig. 1(h) reveals the uniform distribution of five metals throughout every single particle.

As shown in Fig. 2(a), XRD analysis was performed to investigate the structural characteristics of the HELH. The peak of 2θ = 7.3° indicates the residual ZIF-67, while the signals at 12.7°, 25.7°, and 35.2° are characteristic peaks of the HELH phase, with the peak of 35.2° corresponding to the (031) planes as identified in Fig. 1(g). Due to the partial amorphous region, the characteristic peaks are relatively broad and less intense. To definitely exhibit the features of the layered hydroxides, the sample with a fourfold increase in nitrate concentration was prepared through deeper etching, denoted as $HELH_{adj}$. As shown in the SEM images and EDX mapping (Fig. S2 in the ESM), $HELH_{adj}$ still exhibits the lamellar

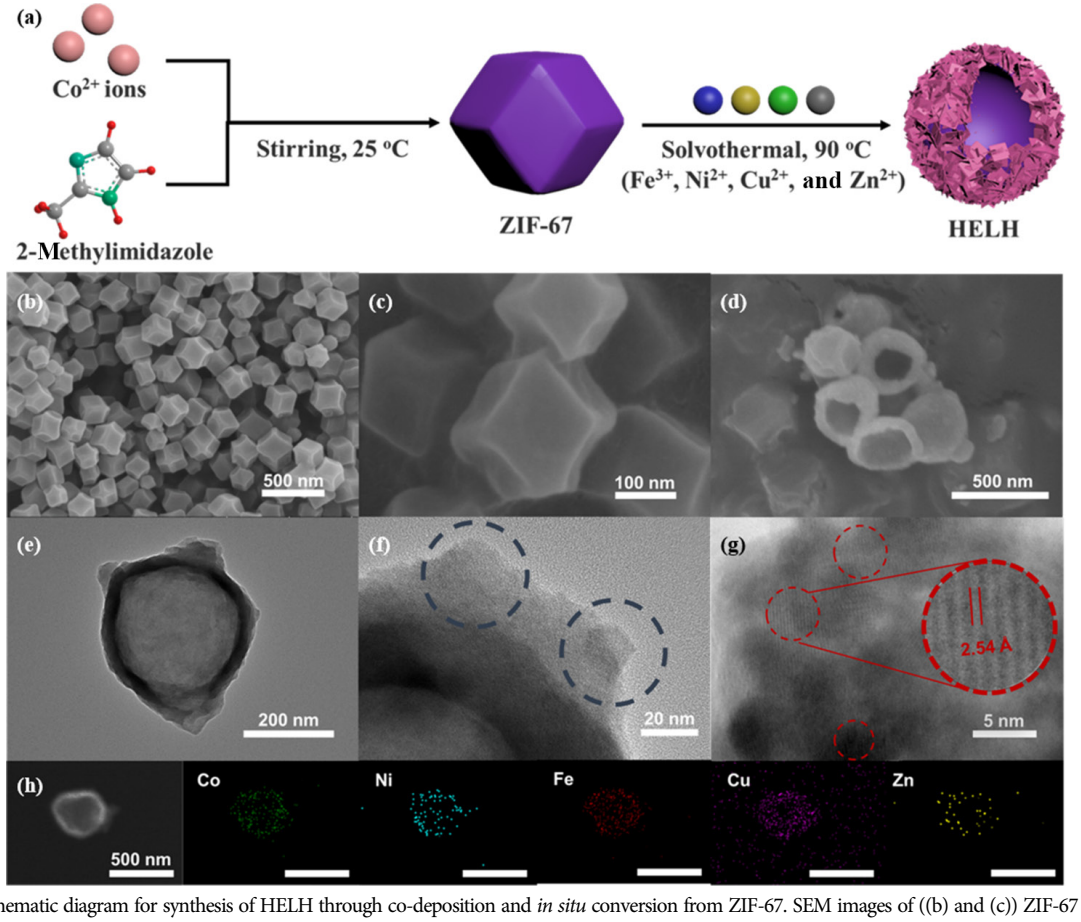

Figure 1 (a) Schematic diagram for synthesis of HELH through co-deposition and *in situ* conversion from ZIF-67. SEM images of ((b) and (c)) ZIF-67 and (d) HELH. (e)–(g) TEM images of HELH. (h) STEM image and EDS elemental mapping of HELH.

morphology with a uniform distribution of metals. With the increasing etching depth, the characteristic peaks of $HELH_{adj}$ are significantly enhanced in the XRD patterns and the signal of ZIF-67 is still distinguishable. Furthermore, compared with reference metal hydroxides (Fig. 2(a) and Fig. S4 in the ESM), it is found that the characteristic peaks of HELH are closest to the standard spectrum of FeO(OH) but shift 1.2° towards a lower angle. This is because the lowest solubility of FeO(OH) leads to preferential nucleation, and the larger radii of the divalent ions than Fe^{3+} cause lattice distortion (Table S2 in the ESM), resulting in an increase in lattice spacing. This distortion generates structural defects that enhance substrate adsorption, while the entropy-stabilized crystal structure strengthens the structural robustness. The FTIR spectra in Fig. 2(b) further verify the residual ZIF-67 in the material. The peak at 1580 cm^{-1} corresponds to the aromatic ring stretching of imidazole, while the peaks at 3130 and 2926 cm^{-1} are attributed to the C–H stretching modes of the aromatic ring and aliphatic chain of imidazole, respectively [40, 41]. The N_2 adsorption/desorption isotherm of HELH from Fig. S5 in the ESM exhibits a typical type I adsorption profile with a hysteresis loop, reflecting a hierarchical micro–mesoporous structure. The pore size distribution curve obviously demonstrates that micro-pores at around 1.2 nm are derived from ZIF-67 [42], and the meso-pores at around 35 nm are stacking pores of layered hydroxides [43]. The electron paramagnetic resonance (EPR) spectra of ZIF-67, HELH and $HELH_{adj}$ were recorded to verify the existence of the oxygen vacancies (Fig. 2(c)). $HELH_{adj}$ shows the most intense signal peak at g = 2.001 attributed to the highest content of hydroxides [44]. Besides, an extra signal with a g = 2.06 appears, which is assigned as surface transition metal ions with the lattice oxygen loss [45]. In the contact angle test as shown in Fig. 2(d), the hydroxides exhibit superior hydrophilicity compared to ZIF-67 (the angle of 35.7° for $HELH_{adj}$), which helps to wet the catalyst surface. Based on the elemental composition of HELH determined by ICP-OES (Table S3 in the ESM), the configurational entropy was calculated ($\Delta S_{conf} = -R\sum x_i \ln x_i$ where R denotes the universal gas constant, and x_i is the mole fraction of the i-th component.) as 1.588R (> 1.5R), confirming the high-entropy nature of materials [46].

XPS was employed to analyze the elemental composition and chemical valence state of the catalyst surface. The survey scan spectrum of HELH confirmed the coexistence of Zn, Co, Ni, Fe, Cu, and O elements (Fig. S6 in the ESM), consistent with the EDS mapping results. As shown in Fig. 3(a), the peak of O 1s is deconvoluted into four peaks at 529.8, 531.2, 532.2, and 533.1 eV, which can be ascribed to lattice oxygen (O4), defect sites with low oxygen coordination (O3), surface hydroxyl group (O2) and adsorbed water (O1), respectively [47]. The high proportion of O3 verifies the material has rich oxygen vacancies, which is beneficial for substrate adsorption. The Fe 2p spectra shown in Fig. 3(b) demonstrates that Fe species exist in the form of Fe^{3+} and Fe^{2+}, while the position of the satellite peak is at 718.3 eV, proving that the main form is Fe^{3+} [48]. Combined with the XRD results, this illustrates a template effect of FeO(OH), which acts as a seed crystal to induce the formation of HELH. The high-resolution Co 2p spectra were fitted to investigate the oxidation states of cobalt (Fig. 3(c)).

The two fitted peaks for Co $2p_{3/2}$ are assigned to Co^{3+} (780.9 eV) and Co^{2+} (782.9 eV), revealing a Co^{3+}/Co^{2+} ratio of 2.44 [46]. In the high-resolution Ni 2p spectrum (Fig. 3(d)), the peaks at 857.3 eV (Ni^{3+}) and 855.5 eV (Ni^{2+}) indicate that the ratio of Ni^{3+}/Ni^{2+} is

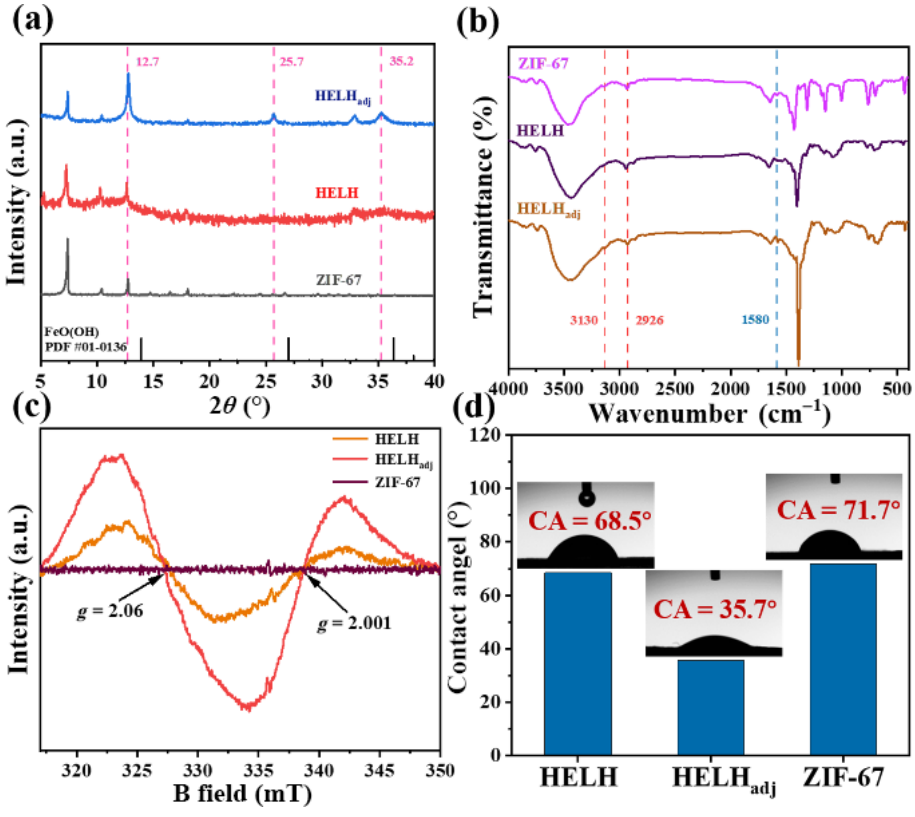

Figure 2 (a) The XRD patterns of ZIF-67, HELH and $HELH_{adj}$. (b) The FT-IR spectra of ZIF-67, HELH and $HELH_{adj}$. (c) The EPR spectra of ZIF-67, HELH and $HELH_{adj}$. (d) Static water contact angle of ZIF-67, HELH and $HELH_{adj}$.

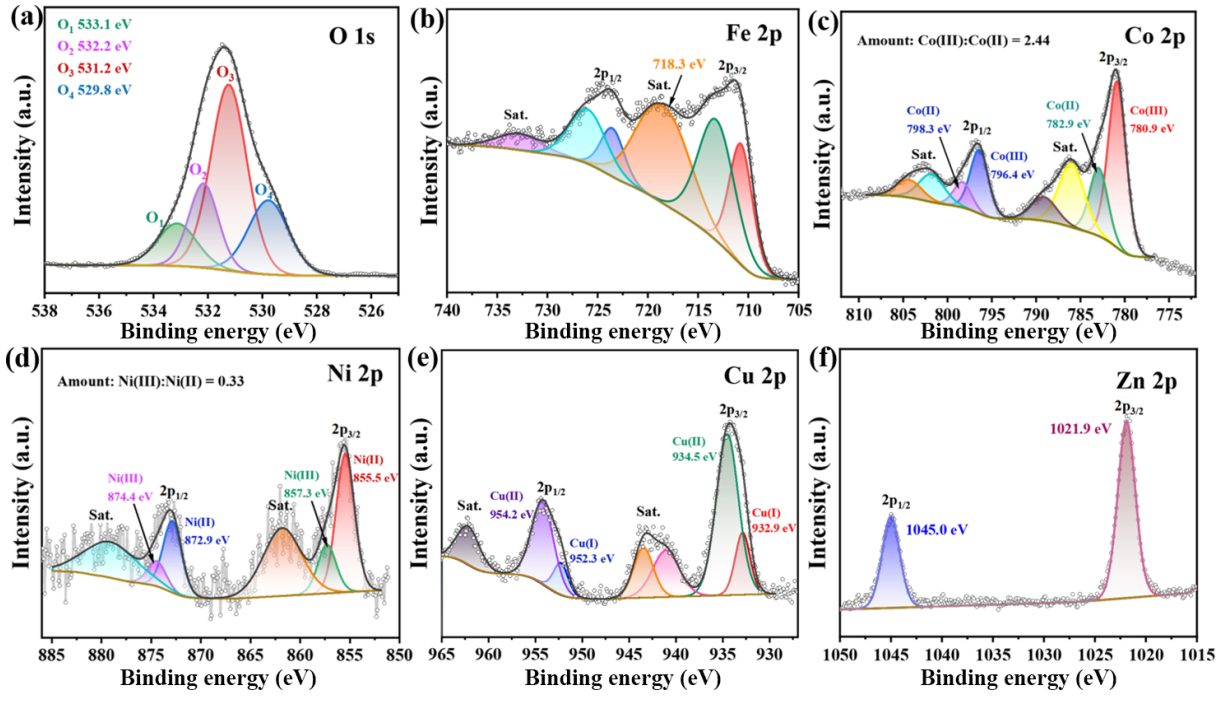

Figure 3 XPS spectra of (a) O 1s, (b) Fe 2p, (c) Co 2p, (d) Ni 2p, (e) Cu 2p, and (f) Zn 2p in HELH.

0.33 [49]. Cobalt and nickel have opposite trivalent and divalent ratios, indicating the layered hydroxide structure. As observed from the Cu 2p spectra in Fig. 3(e), the peak at 934.5 eV is attributed to Cu^{2+}, and the peak at 932.9 eV is assigned to Cu^{+}, likely resulting from the reduction by Ar plasma [47]. Additionally, two characteristic peaks at 1045.0 and 1021.9 eV correspond to Zn^{2+} $2p_{1/2}$ and Zn^{2+} $2p_{3/2}$ [50]. Based on the above characterization, the structure of materials can be identified as HELH hollow nanospheres internally supported by ZIF-67, with iron acting as the template agent for *in-situ* transformation. Moreover, abundant oxygen vacancies and good hydrophilicity of the material can better promote the progress of hydrolysis reactions.

3.2 Catalyst performance test

HELH catalysts were evaluated under a series of concentration gradients to investigate the hydrogen generation at different $NaBH_4$ concentrations. As shown in Figs. 4(a) and 4(b), the hydrogen generation accelerated with increasing concentration in dilute solution (2%–10%), but remained nearly constant at higher concentrations (10%–25%). This preliminarily indicated that the process of $NaBH_4$ hydrolysis followed pseudo-zero-order kinetics in concentrated solutions. Regarding the optimization of catalytic reaction conditions, Fig. 4(c) clearly shows that the hydrogen production increased sharply with the rising reaction temperature. In the absence of catalyst, the hydrogen generation was only 0.15 mL·min^{-1} at 80 °C as shown in the inset of Fig. 4(c). This result indicates that the hydrogen production rate of $NaBH_4$ solution catalyzed by HELH is 400 times faster than spontaneous hydrolysis. Additionally, Fig. 4(d) illustrates the relationship between the hydrolysis rate and NaOH concentration. The hydrogen production rate exhibited a volcano-shaped distribution depending on the concentration of NaOH solution and peaked at 3 M. At higher concentrated NaOH, the hydrolysis of $NaBH_4$ was inhibited. In the absence of catalysts, $NaBH_4$ did not undergo spontaneous decomposition in 5 M NaOH even at 70 °C (inset of Fig. 4(d)). Overall, these performance evaluations demonstrate that $NaBH_4$ exhibits excellent stability in alkaline environments, but it rapidly hydrolyzes upon catalyst addition, highlighting its potential as a stable liquid hydrogen source.

To evaluate the effect of configurational entropy to the hydrogen generation activity, a series of catalysts (Tetra-LH, Tri-LH, and Bi-LH) were synthesized using the same method for comparison with HELH (Figs. 5(a)–5(c)). The results indicate that each material exhibited individually good catalytic activity, but none surpassed HELH. This demonstrates the unique superiority of the high-entropy composition, beyond a simple accumulation of specific metal components. Generally, catalysts containing both Co and Ni displayed enhanced activity, which was further improved by the incorporation of Fe and Zn. Regarding the influence of structure, the performance of HELH, $HELH_{adj}$, and ZIF-67 was compared (Fig. 5(d)). The catalytic activity of ZIF-67 was intermediate between that of HELH and $HELH_{adj}$, which is inconsistent with the positive synergistic effects typically expected from high-entropy materials. This suggests that the outstanding activity of HELH cannot be solely attributed to the presence of multiple metals but also to its unique structural configuration. The SEM images of the catalysts after reaction revealed that HELH retained a relatively intact morphology, whereas $HELH_{adj}$ exhibited significant agglomeration (Figs. S7(a) and S7(b) in the ESM). Therefore, the inferior performance of $HELH_{adj}$ is attributed to the instability of its lamellar structure at elevated temperatures, which reduced the number of exposed active sites and consequently impaired the catalytic activity. These findings underscore that structural robustness also plays a crucial role in catalytic performance, verifying the importance of the reserved MOF core. Furthermore, HELH maintained a high hydrogen generation rate of 6000 mL·min^{-1}·g^{-1} after ten consecutive cycles, demonstrating its long-term stability (Fig. S7(c) in the ESM).

To further elucidate the effect of configurational entropy on catalytic reaction kinetics and thermodynamics, the $NaBH_4$

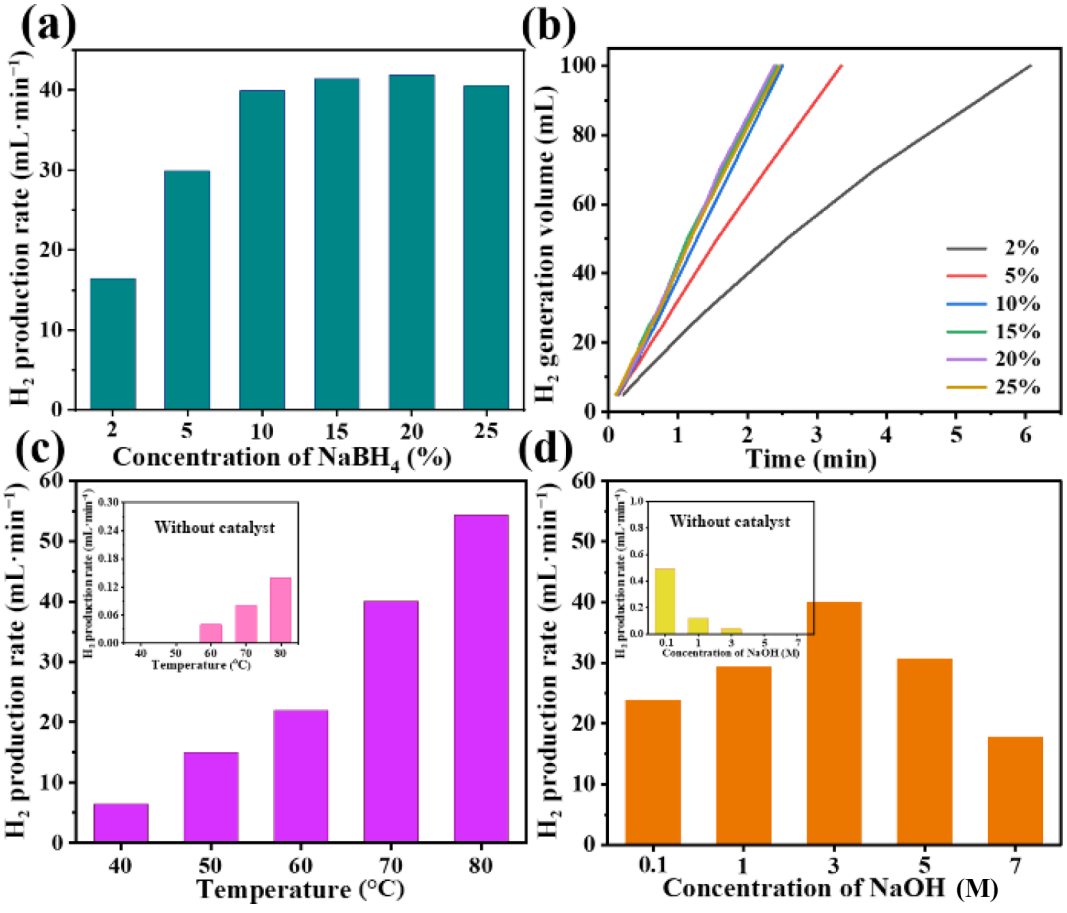

Figure 4 The influence of ((a) and (b)) $NaBH_4$ concentration, (c) temperature, and (d) NaOH concentration on catalytic activity (the inset shows the hydrolysis without catalyst).

hydrolysis activity was investigated over HELH, Tri-LH (CoNiFe, low entropy), and Tetra-LH (CoNiFeZn, medium entropy). As shown in Figs. 6(a)–6(c)), the reactions on all three materials conform to pseudo-zeroth-order kinetics at 50, 60, 70, and 80 °C, indicating the identical reaction pathway. The apparent activation energies (E_a) were derived from the Arrhenius plots for hydrogen production over catalysts (Fig. 6(d)). The E_a with HELH (42.10 ± 3.33 kJ·mol^{-1}) was significantly lower than those with Tetra-LH (50.78 ± 3.33 kJ·mol^{-1}) and Tri-LH (53.88 ± 3.13 kJ·mol^{-1}), demonstrating that higher configurational entropy enhances the catalytic activity. Notably, including the data at 40 °C in the fitting reduced the accuracy of the calculated E_a, as evidenced by a lower R^2 value (0.976, Fig. S8(a) in the ESM). This discrepancy can be attributed to the different dissolution behaviors of the reactant and product at this temperature. As shown in Fig. S8(b) in the ESM, crystals visibly precipitated from the solution during hydrolysis at 40 °C due to solvent (H_2O) consumption and byproduct ($NaBO_2$) formation, even though the reactant ($NaBH_4$) was initially fully dissolved before the reaction. Therefore, the hydrolysis of concentrated $NaBH_4$ should be maintained at a relatively high temperature to prevent the precipitation of $NaBO_2$ on the catalyst surface, which would block the active sites and hinder the contact with the reactants.

3.3 Catalytic mechanism analysis

According to previous reports [51, 52], hydrogen generation in the $NaBH_4$ hydrolysis reaction proceeds via cleavage of the B–H bond in BH_4^- to form $H^{\delta-}$, which subsequently reacts with H_2O, resembling the hydrogen evolution reaction (HER). To further explore the electron transfer from $H^{\delta-}$ to H_2O, the materials were evaluated following the HER test of the electrocatalysts. As shown in Fig. 7(a), the electrochemical activities of ZIF-67, Tri-LH (CoNiFe, low entropy), and HELH were assessed by linear sweep voltammetry (LSV) in a 3 M NaOH solution at a scan rate of 0.2 mV·s^{-1}. ZIF-67 exhibited the highest overpotential (0.46 V) at 30 mA·cm^{-2}, significantly greater than those of HELH (0.34 V) and Tri-LH (0.36 V). The superior HER activity of HELH is attributable to the favorable hydrophilicity of the layered hydroxides and their abundant oxygen vacancies, which facilitate H_2O adsorption. This result indicates the efficacy of layered hydroxides in promoting H_2O reduction by lowering the effective energy barrier, which is consistent with the enhanced performance observed in $NaBH_4$ hydrolysis. To gain further insight into the reaction kinetics, Tafel slope analysis was conducted in the kinetic region of the LSV near the onset potential (Fig. 7(b)). All three materials exhibited Tafel slopes greater than 30 mV·dec^{-1}, confirming that the HER process follows the Volmer–Heyrovsky mechanism in which $H^{\delta-}$ directly reacts with H_2O. Additionally, the Tafel slopes followed the order: HELH < Tri-LH < ZIF-67, verifying the fastest charge transfer kinetics for HELH, which aligns with the trend observed in the activation energies for $NaBH_4$ hydrolysis. These consistencies reveal a strong similarity in the active sites and mechanisms between chemical hydrogen production via $NaBH_4$ hydrolysis and HER. Moreover, electrochemical impedance spectroscopy (EIS) was

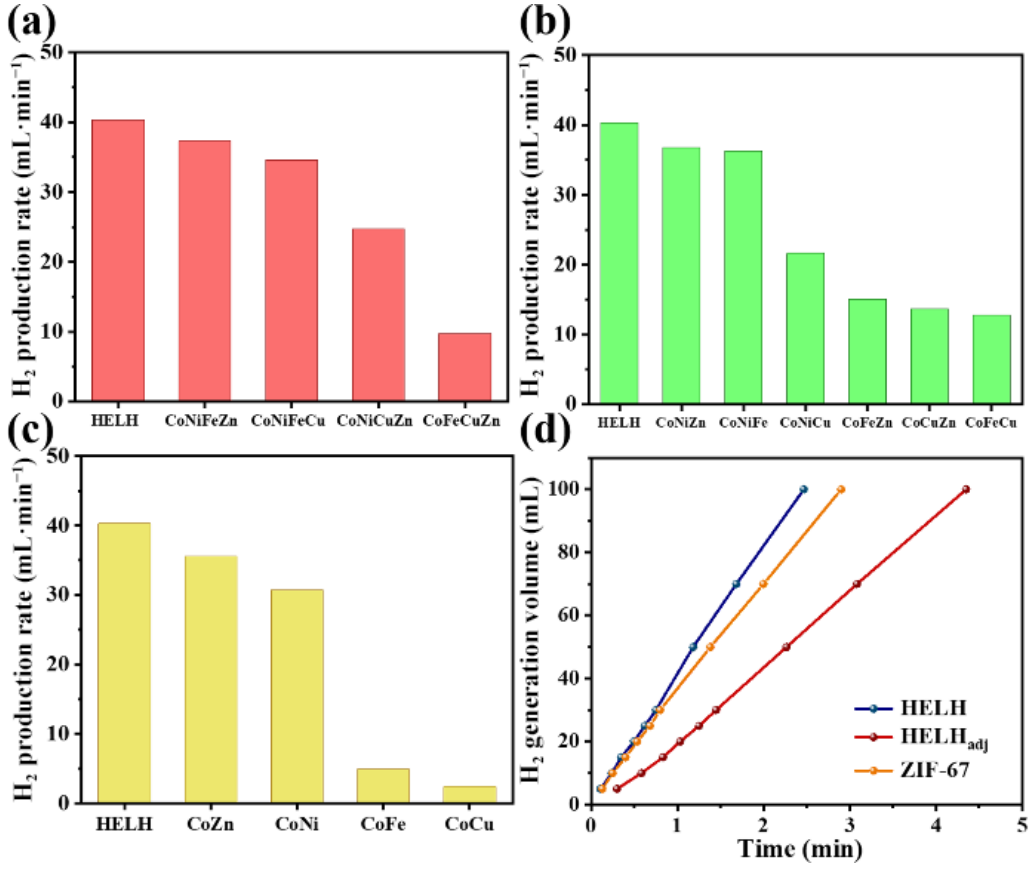

Figure 5 The catalytic activity comparison of HELH with (a) Tetra-LH, (b) Tri-LH, (c) Bi-LH, and (d) $HELH_{adj}$ and ZIF-67.

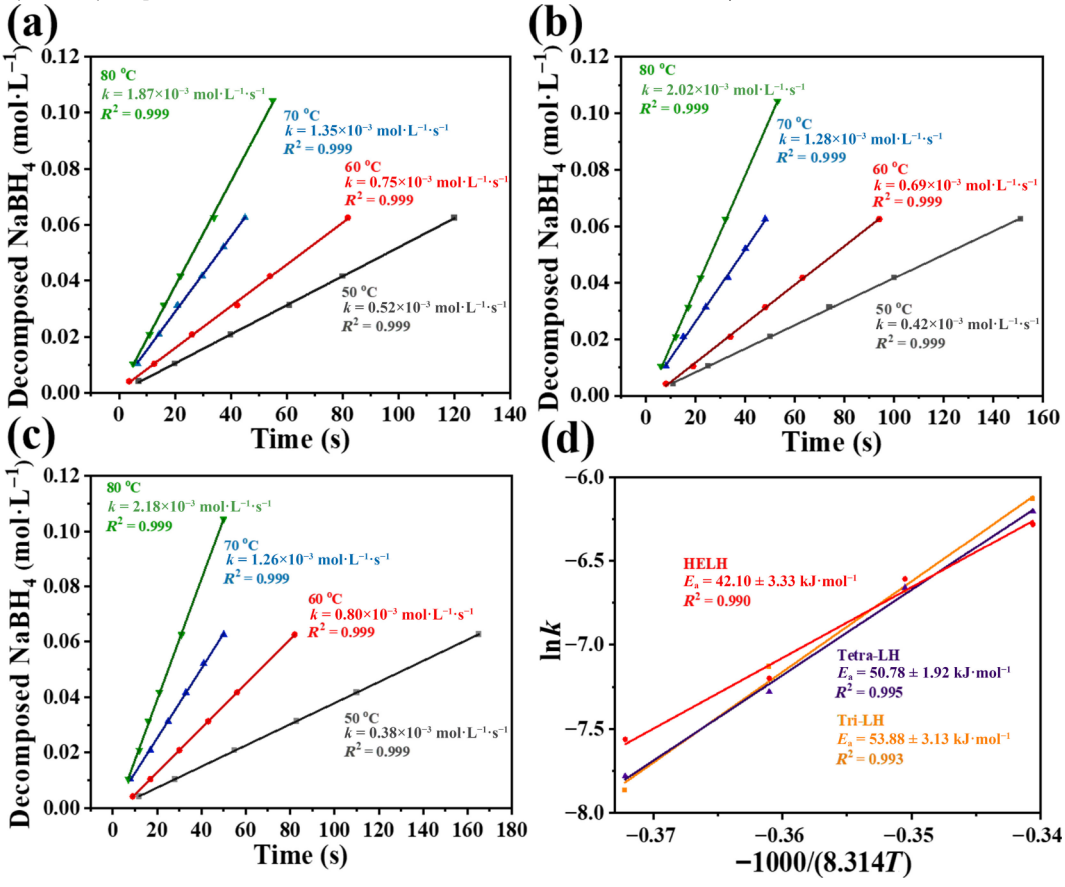

Figure 6 The pseudo-zero-order fitting of (a) HELH, (b) Tri-LH (CoNiFe), and (c) Tetra-LH (CoNiFeZn). (d) Arrhenius plot for hydrogen production with catalysts.

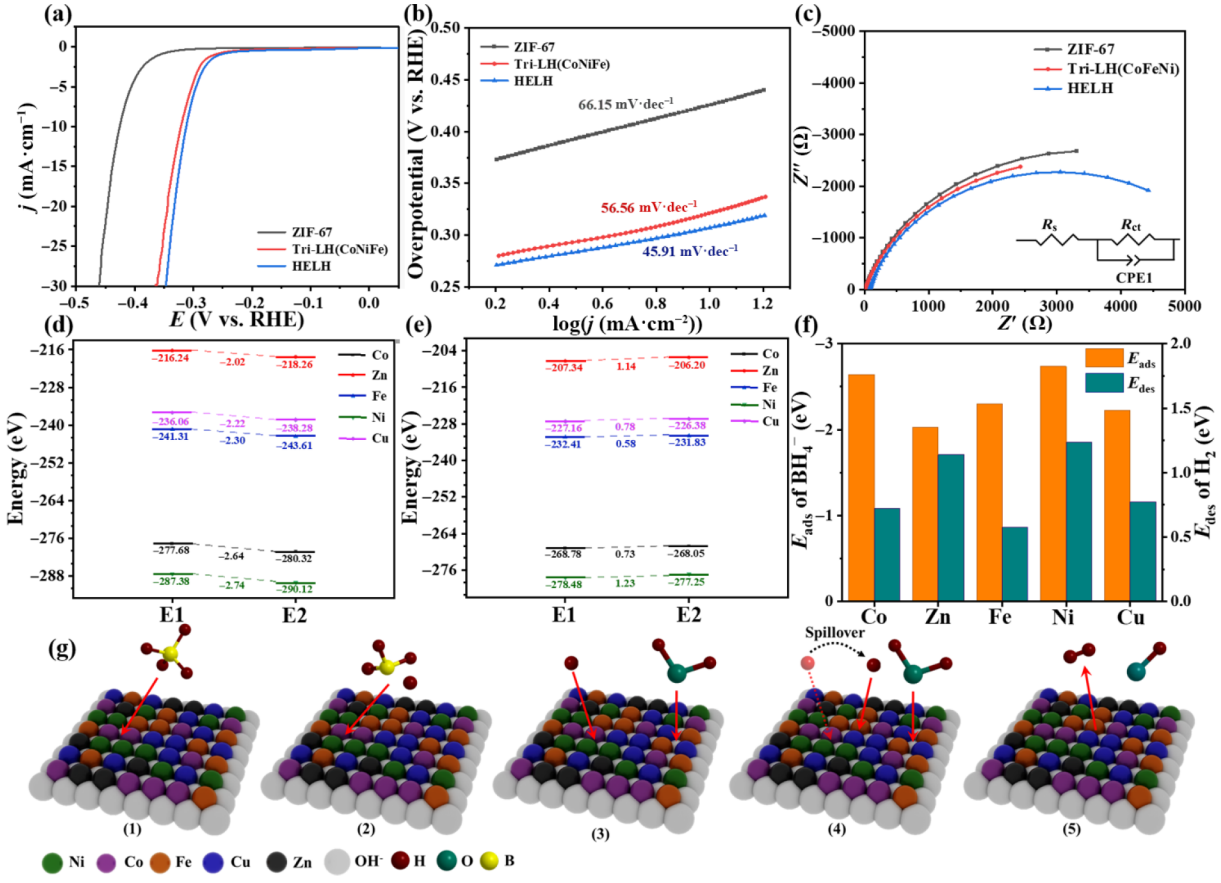

Figure 7 (a)–(c) Electrochemical analysis of HELH, Tri-LH (CoNiFe), and ZIF-67: (a) linear sweep voltammetry (LSV) curves in 3 M NaOH electrolyte; (b) corresponding Tafel plots; (c) electrochemical impedance spectroscopic analysis in 3 M NaOH electrolyte. (d) Adsorption energy of BH_4^- on five metals. (e) Desorption energy of H_2 on five metals. (f) Comparison of E_{ads} and E_{des} on five metals. (g) Schematic representation of hydrolysis mechanism.

employed to investigate the charge transfer resistance (Fig. 7(c), inset shows the equivalent circuit). The Nyquist plots for all materials exhibited a semicircular shape, where the diameter corresponds to the charge transfer resistance (R_{ct}). HELH displayed the smallest semicircle, indicating the lowest R_{ct}, which demonstrates that the high-entropy structure facilitates rapid electron transfer. However, the relatively large R_{ct} values observed for all materials further suggest that $H^{\delta-}$ directly reacts with H_2O. Hence, the efficient interaction between $H^{\delta-}$ (generated from BH_4^-) and H_2O is particularly crucial for the hydrolysis reaction.

To elucidate the catalytic mechanism of HELH, the hydrogen generation pathway from $NaBH_4$ was investigated with density functional theory (DFT) calculation, which simulates the production and consumption processes of $H^{\delta-}$. The adsorption energies of BH_4^- on the five metal sites are shown in Figs. 7(d) and 7(f) and Fig. S9 in the ESM. The lowest energies on Co (−2.64 eV) and Ni (−2.74 eV) indicate that BH_4^- preferentially adsorbs on these sites and subsequently decomposes to generate $H^{\delta-}$. Similarly, the calculation results reveal that H_2 tends to desorb from Fe, Co, and Cu, as their desorption energies of H_2 are 0.58, 0.73, and 0.78 eV, respectively (Figs. 7(e) and 7(f) and Fig. S10 in the ESM). Combining simulation and experimental results, a plausible catalytic mechanism for HELH in concentrated $NaBH_4$ solution can be proposed as illustrated in Fig. 7(g): (1) BH_4^- is preferentially adsorbed on Ni and Co sites due to the favorable adsorption energy; (2) the B–H bond in BH_4^- cleaves to generate $H^{\delta-}$; (3) H_2O is adsorbed at oxygen vacancies in the catalyst; (4) owing to the uniform element distribution in the high-entropy material, the active H species undergoes surface spillover [53, 54], migrating from Ni/Co sites to Fe/Cu sites; (5) $H^{\delta-}$ reacts with the adsorbed H_2O, and H_2 is released from Fe and Cu sites. Furthermore, the presence of Zn^{2+}, which has the largest ionic radius (Table S2 in the ESM), enhances lattice distortion, promoting the formation of more oxygen vacancies and thereby accelerating step (3). In summary, the synergistic interplay among the elements in the high-entropy material optimizes the hydrolysis pathway, which lowers the activation energy and enhances the long-term durability of the catalyst.

3.4 Application in continuous flow reactor

Finally, a prototype hydrogen supply unit for fuel cells was designed, as shown in Fig. S11 in the ESM. The reactor adopted a plate-type configuration, in which a silicone gasket served both as a seal and as a flow channel for the reaction mixture. A gas–liquid separator was positioned downstream of the reactor to preliminarily separate the generated mixture, after which the hydrogen was directed into the fuel cell through a drying tube. To effectively utilize the catalyst, customized materials were prepared by loading ZIF-67 onto nickel foam and subsequently converting it into HELH (Figs. 8(a)–8(c)). The reactor performance was evaluated under a flow rate of 2 mL·min^{-1} at 70 °C (Fig. 8(d)). The hydrogen production rate reached a maximum of 4.16 L·min^{-1}·g^{-1} after approximately 10 min of activation. After 100 min, the catalyst activity gradually declined, with the hydrogen generation decreasing by only 21% at the 120-min mark. This study successfully demonstrates the feasibility of HELH in practical scenarios.

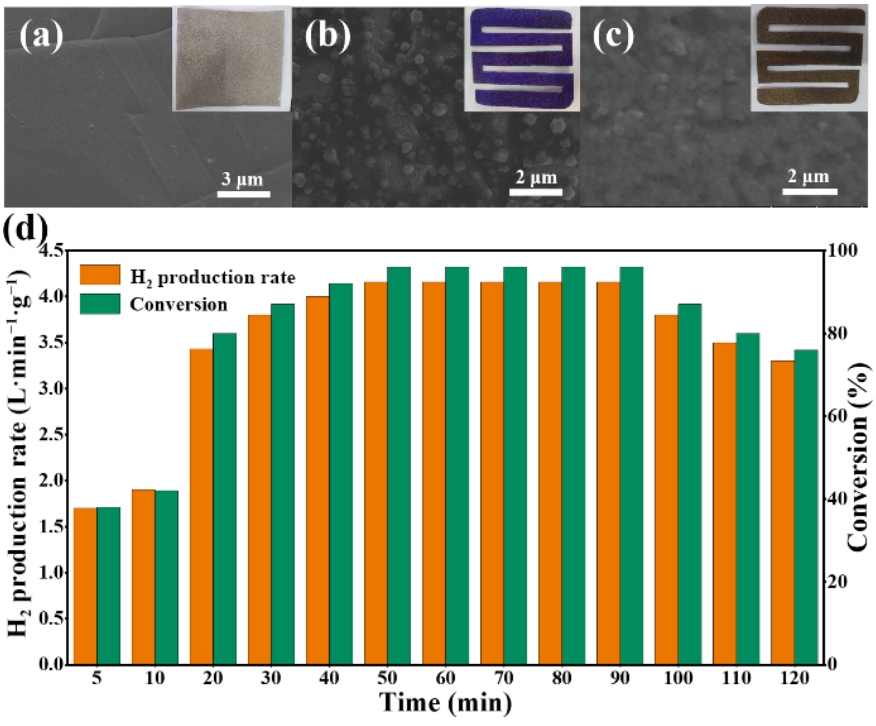

Figure 8 SEM images and physical pictures of (a) Ni foam, (b) ZIF-67/NF, and (c) HELH/NF. (d) Long-term hydrogen production performance.

4 Conclusions

In summary, we synthesized a hollow nano-spherical HELH catalyst via the *in-situ* etching conversion of ZIF-67. This catalyst demonstrates high efficiency and robust stability for hydrogen generation from concentrated $NaBH_4$ solutions. The retained built-in MOF framework reinforces the active high-entropy hydroxide shell, maintaining both activity and structural stability. Combining catalyst performance, simulated calculations, and electrochemical analysis, it was found that the multi-metal synergy and abundant oxygen vacancies in HELH optimize the hydrolysis pathway through facilitating charge transfer and reducing the activation energy. Consequently, the catalyst achieved a hydrogen generation rate of 8 $L{\cdot}min^{-1}{\cdot}g^{-1}$ in 25 wt.% $NaBH_4$ with 3 M NaOH solution at 70 °C and retained stable performance after 10 cycles. A prototype hydrogen generation module based on this catalyst was fabricated and stably operated for at least 2 h with 3.3 $L{\cdot}min^{-1}{\cdot}g^{-1}$ H_2 production, highlighting the potential of HELH catalyst for practical hydrogen-on-demand systems.

Electronic Supplementary Material: Supplementary material (electrochemical measurements, DFT calculations, supplementary characterization and explanatory notes for relevant materials, catalyst cycling performance tests, calculation simulation model diagrams, and physical pictures of the reaction device) is available in the online version of this article at https://doi.org/10.26599/NR.2026.94908464.

Data availability

All data needed to support the conclusions in the paper are presented in the manuscript and/or the Electronic Supplementary Material. Additional data related to this paper may be requested from the corresponding author upon request.

Acknowledgements

This work was financially supported by the National Natural Science Foundation of China (Nos. 22304099, 82304442, and 82574366).

Declaration of competing interest

All the contributing authors report no conflict of interests in this work.

Author contribution statement

X. C.: Conducted methodology design, formal analysis, contributed to writing, review, and editing of the manuscript. Z. Y. W.: Contributed to conceptualization, participated in review, and editing of the manuscript. H. Y.: Performed formal analysis and experimental investigation. M. J. J.: Carried out formal analysis and contributed to conceptualization. Y. M. W.: Responsible for data curation and project supervision. D. S.: Performed experimental investigation. N. J.: Contributed to software-related work. Y. W.: Participated in methodology design. Z. L. L.: Contributed to methodology design. G. W. X.: Conducted software-related work. Y. J. A.: Acquired funding. H.-B. S.: contributed to methodology design, supervision, and manuscript review and editing.

Use of AI statement

None.

References

[1] Tian, W. Y.; Zhang, X. H.; Zhou, P.; Guo, R. X. Review of energy management technologies for unmanned aerial vehicles powered by hydrogen fuel cell. *Energy* **2025**, *323*, 135751.

[2] Shen, W.; Peng, J. Z.; Ma, R.; Wu, J. Q.; Li, J. Y.; Liu, Z. W.; Leng, J.

M.; Yan, X. J.; Qi, M. J. Sunlight-powered sustained flight of an ultralight micro aerial vehicle. *Nature* **2024**, *631*, 537–543.
[3] Wang, Z. X.; Liu, Z.; Fan, L. H.; Du, Q.; Jiao, K. Application progress of small-scale proton exchange membrane fuel cell. *Energy Rev.* **2023**, *2*, 100017.
[4] Tan, Z. H.; Ouyang, L. Z.; Huang, J. M.; Liu, J. W.; Wang, H.; Shao, H. Y.; Zhu, M. Hydrogen generation via hydrolysis of Mg_2Si. *J. Alloys Compd.* **2019**, *770*, 108–115.
[5] Ma, M. L.; Yang, L. L.; Ouyang, L. Z.; Shao, H. Y.; Zhu, M. Promoting hydrogen generation from the hydrolysis of Mg-graphite composites by plasma-assisted milling. *Energy* **2019**, *167*, 1205–1211.
[6] Tan, Z. H.; Ouyang, L. Z.; Liu, J. W.; Wang, H.; Shao, H. Y.; Zhu, M. Hydrogen generation by hydrolysis of Mg–Mg_2Si composite and enhanced kinetics performance from introducing of $MgCl_2$ and Si. *Int. J. Hydrogen Energy* **2018**, *43*, 2903–2912.
[7] Huang, M. H.; Ouyang, L. Z.; Chen, Z. L.; Peng, C. H.; Zhu, X. K.; Zhu, M. Hydrogen production via hydrolysis of Mg-oxide composites. *Int. J. Hydrogen Energy* **2017**, *42*, 22305–22311.
[8] Wei, X. Y.; Sharma, S.; Waeber, A.; Wen, D.; Margni, M.; Maréchal, F.; Van Herle, J. Environmental implications of solid oxide fuel cell system for hydrogen sustainability. *Resour., Conserv. Recycl.* **2025**, *215*, 108134.
[9] Kim, D.; Oh, S.; Kim, Y.; Park, J. Sustainable hydrogen production via carbon black: Direct carbon fuel cell application for turquoise hydrogen. *Chem. Eng. J.* **2025**, *511*, 162056.
[10] Grenko, B.; de Jong, W.; van de Ketterij, R.; van Biert, L. Dynamic modelling of methanol steam reforming to hydrogen in a packed bed reactor for shipboard fuel cells. *Chem. Eng. J.* **2025**, *507*, 160623.
[11] Guo, Q.; Wang, X. L.; Yang, F.; Zhou, S. H.; Wei, K. X.; Zhang, Y.; Sun, L.; Sun, S. Y.; Liu, H. C.; An, J. P. et al. Pt single-atomic-site loaded on borate anion-intercalated $Co(OH)_2$ nanoflakes for enhanced hydrogen generation dynamics of $NaBH_4$ hydrolysis. *Chem. Eng. J.* **2025**, *516*, 164141.
[12] Liu, X.; Sun, W.; Chen, J. X.; Wen, Z. H. Controllable electrochemical liberation of hydrogen from sodium borohydride. *Angew. Chem., Int. Ed.* **2024**, *63*, e202317313.
[13] Ouyang, L. Z.; Jiang, J.; Chen, K.; Zhu, M.; Liu, Z. W. Hydrogen production via hydrolysis and alcoholysis of light metal-based materials: A review. *Nano-Micro Lett.* **2021**, *13*, 134.
[14] Ouyang, L. Z.; Chen, W.; Liu, J. W.; Felderhoff, M.; Wang, H.; Zhu, M. Enhancing the regeneration process of consumed $NaBH_4$ for hydrogen storage. *Adv. Energy Mater.* **2017**, *7*, 1700299.
[15] Zhu, Y. Y.; Ouyang, L. Z.; Zhong, H.; Liu, J. W.; Wang, H.; Shao, H. Y.; Huang, Z. G.; Zhu, M. Closing the loop for hydrogen storage: Facile regeneration of $NaBH_4$ from its hydrolytic product. *Angew. Chem., Int. Ed.* **2020**, *59*, 8623–8629.
[16] Chen, K.; Zhong, H.; Ouyang, L. Z.; Liu, F.; Wang, H.; Liu, J. W.; Shao, H. Y.; Zhu, M. Achieving a novel solvent-free regeneration of $LiBH_4$ combining hydrogen storage and production in a closed material cycle. *J. Magnesium Alloys* **2023**, *11*, 1697–1708.
[17] Patel, N.; Patton, B.; Zanchetta, C.; Fernandes, R.; Guella, G.; Kale, A.; Miotello, A. Pd–C powder and thin film catalysts for hydrogen production by hydrolysis of sodium borohydride. *Int. J. Hydrogen Energy* **2008**, *33*, 287–292.
[18] Onat, E.; İzgi, M. S.; Şahin, Ö.; Ekinci, S. Enhanced hydrogen production from sucrose-derived carbon quantum dots-supported Ru catalysts: A comparative study of KBH_4 and $NaBH_4$ hydrolysis. *Renew. Energy* **2025**, *254*, 123692.
[19] Coşkuner Filiz, B.; Kantürk Figen, A. Insight into the role of solvents in enhancing hydrogen production: Ru–Co nanoparticles catalyzed sodium borohydride dehydrogenation. *Int. J. Hydrogen Energy* **2019**, *44*, 28471–28482.
[20] Kilinc, D.; Sahin, O. Highly active and stable CeO_2 supported nickel-complex catalyst in hydrogen generation. *Int. J. Hydrogen Energy* **2021**, *46*, 499–507.
[21] Nabid, M. R.; Bide, Y.; Kamali, B. Hydrogen release from sodium borohydride by Fe_2O_3@nitrogen-doped carbon core–shell nanosheets as reasonable heterogeneous catalyst. *Int. J. Hydrogen Energy* **2019**, *44*, 25662–25670.
[22] Didehban, A.; Zabihi, M.; Shahrouzi, J. R. Experimental studies on the catalytic behavior of alloy and core–shell supported Co–Ni bimetallic Nano-catalysts for hydrogen generation by hydrolysis of sodium borohydride. *Int. J. Hydrogen Energy* **2018**, *43*, 20645–20660.
[23] Krishnan, P.; Hsueh, K. L.; Yim, S. D. Catalysts for the hydrolysis of aqueous borohydride solutions to produce hydrogen for PEM fuel cells. *Appl. Catal. B: Environ.* **2007**, *77*, 206–214.
[24] Sahiner, N.; Ozay, O.; Inger, E.; Aktas, N. Superabsorbent hydrogels for cobalt nanoparticle synthesis and hydrogen production from hydrolysis of sodium boron hydride. *Appl. Catal. B: Environ.* **2011**, *102*, 201–206.
[25] Wang, Y. N.; Zheng, X. P.; Xu, B.; Liu, Y. J.; Xia, Z. W. Hydrogen generation by hydrolysis of alkaline $NaBH_4$ solution doped with amorphous catalyst Co–Y_2O_3–B/CNTs. *Int. J. Hydrogen Energy* **2024**, *69*, 1492–1500.
[26] Yurderi, M. PtCo/g-C_3N_4 bimetallic catalyst: Boosting hydrogen production in sodium borohydride hydrolysis. *Int. J. Hydrogen Energy* **2025**, *143*, 105–111.
[27] Zhao, W.; Zhang, Z.; Li, Z. J.; Zhang, Y. J.; Wang, C.; Han, L.; Guo, J.; Hu, X. M.; Peng, C.; Ramakrishna, S. et al. Regulating the electronic structure of dual active site Co/MoO_x-cCNT for catalyzing $NaBH_4$ hydrolysis towards controllable high-capacity hydrogen production. *Chem. Eng. J.* **2025**, *505*, 159274.
[28] Onat, E.; Celik, F. A.; Karabulut, E.; Izgi, M. S. High availability and outstanding catalytic activity in sodium borohydride hydrolytic dehydrogenation of CQD/GO@Co catalyst by green synthesis: Experimental and computational perspective. *Int. J. Hydrogen Energy* **2024**, *83*, 903–915.
[29] Wei, S. L.; Kim, S. J.; Kang, J. Y.; Zhang, Y.; Zhang, Y. J.; Furuhara, T.; Park, E. S.; Tasan, C. C. Natural-mixing guided design of refractory high-entropy alloys with as-cast tensile ductility. *Nat. Mater.* **2020**, *19*, 1175–1181.
[30] Ai, Y. J.; He, M. Q.; Sun, H.; Jia, X. M.; Wu, L.; Zhang, X. Y.; Sun, H. B.; Liang, Q. L. Ultra-small high-entropy alloy nanoparticles: Efficient nanozyme for enhancing tumor photothermal therapy. *Adv. Mater.* **2023**, *35*, 2302335.
[31] Li, Q. Q.; Wang, F.; Liu, X. Y.; Xu, W. H.; Zhang, K. Y.; Zhang, S. Y.; Teng, P. F.; Zhang, L. L. An infrared radiation-responsive high-entropy CoCaMgMnAlFe-LDHs for controllable hydrogen generation via $NaBH_4$ hydrolysis: Utilization of steel slag and lithium-ion battery liquid waste. *Chem. Eng. J.* **2024**, *500*, 157380.
[32] Li, Q. Q.; Xu, W. H.; Dai, K.; Miao, T. F.; Zou, Y. L.; Wang, N. J.; Sun, X. J.; Li, X.; Zhang, L. L. Ultraviolet–visible–near-infrared irradiation responsive high-entropy layered double hydroxides for on-demand hydrogen evolution reaction via sodium borohydride hydrolysis. *Renew. Energy* **2025**, *249*, 123227.
[33] Qiao, H. M.; Yang, H. T.; Han, Y. D.; Liu, Y. F.; Zhang, Y.; Zhang, X. Excellent laccase-like activity of melamine modified Cu–NH_2-BDC and selective sensing analyses toward phenols and amines. *Nano Res.* **2024**, *17*, 9887–9897.
[34] Rossin, A.; Tuci, G.; Luconi, L.; Giambastiani, G. Metal-organic frameworks as heterogeneous catalysts in hydrogen production from lightweight inorganic hydrides. *ACS Catal.* **2017**, *7*, 5035–5045.
[35] Deonikar, V. G.; Rajkamal, A.; Kim, H. 3D hollow microrod engineered MOF-derived Cu/Co catalysts promoted by Al nanoflakes for efficient H_2 generation through $NaBH_4$ hydrolysis: Perceptions on boosted reaction channels aided by a synergistic effect. *Sustain. Mater. Technol.* **2023**, *38*, e00711.
[36] Zhao, M. M.; Wang, D.; Kang, H. G.; Shi, Z. N.; Hu, X. W.; Sun, H. B.; Xu, J. L. Oxygen-vacancy rich multi-level morphology HEO for high catalytic performance oxygen evolution reactions. *Chem. Commun.* **2025**, *61*, 15866–15869.
[37] Dong, W. Y.; Liu, Z. S.; Sun, H. B.; Shi, Z. N.; Xu, J. L. Ultrathin

defect-rich nanosheets of NiFe-MOF with high specific capacitance and stability for supercapacitor. *Mater. Today Chem.* **2024**, *36*, 101938.

[38] Yue, K. H.; Lu, R. H.; Gao, M. B.; Song, F.; Dai, Y.; Xia, C. F.; Mei, B. B.; Dong, H. L.; Qi, R. J.; Zhang, D. L. et al. Polyoxometalated metal-organic framework superstructure for stable water oxidation. *Science* **2025**, *388*, 430–436.

[39] Andres-Garcia, E.; Oar-Arteta, L.; Gascon, J.; Kapteijn, F. ZIF-67 as silver-bullet in adsorptive propane/propylene separation. *Chem. Eng. J.* **2019**, *360*, 10–14.

[40] Zhou, H. J.; Zheng, M. B.; Tang, H.; Xu, B. Y.; Tang, Y.; Pang, H. Amorphous intermediate derivative from ZIF-67 and its outstanding electrocatalytic activity. *Small* **2020**, *16*, 1904252.

[41] Chen, M. T.; Wang, N.; Wang, X. B.; Zhou, Y.; Zhu, L. H. Enhanced degradation of tetrabromobisphenol A by magnetic Fe_3O_4@ZIF-67 composites as a heterogeneous Fenton-like catalyst. *Chem. Eng. J.* **2021**, *413*, 127539.

[42] Wu, H. Y.; Qian, X. K.; Zhu, H. P.; Ma, S. H.; Zhu, G. S.; Long, Y. Controlled synthesis of highly stable zeolitic imidazolate framework-67 dodecahedra and their use towards the templated formation of a hollow Co_3O_4 catalyst for CO oxidation. *RSC Adv.* **2016**, *6*, 6915–6920.

[43] Yang, K.; Huang, Y. L.; Wang, P. X.; Tang, Y. X.; Zhu, Y. W.; Zhu, X. X.; Xu, Y.; Jiang, W.; Pan, L. M.; Li, Q. et al. LDH nanocrystal@amorphousness core-shell structure derived from LDH→LDO transformation: Synergistically enhanced energy stored for LIBs anode. *Chem. Eng. J.* **2024**, *486*, 150416.

[44] Zhang, J. B.; Yin, R. G.; Shao, Q.; Zhu, T.; Huang, X. Q. Oxygen vacancies in amorphous InO_x nanoribbons enhance CO_2 adsorption and activation for CO_2 electroreduction. *Angew. Chem., Int. Ed.* **2019**, *58*, 5609–5613.

[45] Chen, B. F.; Meng, Z. Y.; Ouyang, P.; Duan, Y. Y.; Li, Y. H.; Wang, W. J.; Dong, F. S_2-doping inducing self-adapting dual anion defects in $ZnSn(OH)_6$ for highly efficient photoactivity. *Appl. Catal. B: Environ.* **2023**, *338*, 123093.

[46] Yeh, J. W. Alloy design strategies and future trends in high-entropy alloys. *JOM* **2013**, *65*, 1759–1771.

[47] Gu, K. Z.; Zhu, X. Y.; Wang, D. D.; Zhang, N. N.; Huang, G.; Li, W.; Long, P.; Tian, J.; Zou, Y. Q.; Wang, Y. Y. et al. Ultrathin defective high-entropy layered double hydroxides for electrochemical water oxidation. *J. Energy Chem.* **2021**, *60*, 121–126.

[48] Biesinger, M. C.; Payne, B. P.; Grosvenor, A. P.; Lau, L. W. M.; Gerson, A. R.; Smart, R. S. C. Resolving surface chemical states in XPS analysis of first row transition metals, oxides and hydroxides: Cr, Mn, Fe, Co and Ni. *Appl. Surf. Sci.* **2011**, *257*, 2717–2730.

[49] Meng, J. M.; Song, Y.; Qin, Z. M.; Wang, Z. H.; Mu, X. J.; Wang, J.; Liu, X. X. Cobalt-nickel double hydroxide toward mild aqueous zinc-ion batteries. *Adv. Funct. Mater.* **2022**, *32*, 2204026.

[50] Ding, Y. R.; Wang, Z. Y.; Liang, Z. J.; Sun, X. P.; Sun, Z. H.; Zhao, Y. X.; Liu, J. L.; Wang, C. Y.; Zeng, Z. Y.; Fu, L. et al. A monolayer high-entropy layered hydroxide frame for efficient oxygen evolution reaction. *Adv. Mater.* **2025**, *37*, 2302860.

[51] Guo, J. Y.; Wang, B. Z.; Yang, D. D.; Wan, Z. X.; Yan, P. X.; Tian, J. N.; Isimjan, T. T.; Yang, X. L. Rugae-like Ni_2P–CoP nanoarrays as a bi-functional catalyst for hydrogen generation: $NaBH_4$ hydrolysis and water reduction. *Appl. Catal. B: Environ.* **2020**, *265*, 118584.

[52] Zhou, S. Q.; Cheng, L. R.; Huang, Y.; Liu, Y.; Shi, L. Y.; Isimjan, T. T.; Yang, X. L. Constructing Ru particles decorated Co_3B-CoP heterostructures as a highly active and reusable catalyst for H_2 generation by catalyzing $NaBH_4$ hydrolysis. *Appl. Catal. B: Environ.* **2023**, *328*, 122519.

[53] Akhound, M. A.; Jacobsen, K. W.; Thygesen, K. S. Activating the basal plane of 2D transition metal dichalcogenides via high-entropy alloying. *J. Am. Chem. Soc.* **2025**, *147*, 5743–5754.

[54] Shun, K.; Mori, K. Unlocking hydrogen spillover: Dynamic behavior and advanced applications. *Acc. Chem. Res.* **2025**, *58*, 3060–3070.